Determination of Parameters of Time-delayed Embedding Algorithm Using Koopman Operator-based Model Predictive Frequency Control

Xiawen Li, *Member, IEEE*, Chetan Mishra, *Member, IEEE*, Shichao Chen, Yajun Wang, *Senior Member, IEEE*, and Jaime De La Ree

***Abstract*—Power systems around the world have been registering a degenerating inertial response in view of the growth of inverter-based resources along with the withdrawal of conventional coal units. Therefore, there is a need for swift frequency support and its control, preferably by means of power electronic-interfaced storage devices, owing to their beneficial capabilities. Despite being particularly efficient, pragmatically, the traditional model-based non-linear control techniques are not highly popular in power system control design, primarily due to the complications faced in obtaining accurately suitable models for certain power system components. Lately, the model-free Koopman operator-based model predictive control (KMPC) has proven to be highly conducive for data-driven non-linear control design. The principle behind KMPC is to change the coordinates in a manner to get an approximately linear model, which can then be controlled using a linear model predictive control. In this study, we employed time-delayed embedding of measurements to reconstruct a new set of preferable coordinates, thereby suggesting an approach for finding the optimal number of time lags and the embedding dimensions which are the key parameters of this algorithm. The efficacy of this KMPC framework is established by adopting a decentralized frequency control problem through a decoupled synchronous machine system, which we proposed for both the Kundur two-area system as well as the IEEE 39-bus test system.**

***Index Terms*—False nearest neighbors, koopman operator, model predictive control, non-linear control, time-delayed embedding.**

I. Introduction

THE mounting implementation of inverter-based resources (IBRs) in worldwide power systems of late has resulted in a deteriorating tendency in overall system inertia [1], [2] giving rise to critical reliability concerns, especially for transient and frequency stability. Although frequency support can be derived from the IBRs by allotting some headroom in the real power output, this comes at a cost of underutilizing the available resources [3]. Nevertheless, an extensive amount of research has been undertaken on the exploration of grid support functionalities of IBRs. Shekhar *et al*. [4] operated PV (Photovoltaic) at an off-MPPT (Maximum Power Point Tracker) output aiming to retain reserved power to regulate frequency. The investigations in [1], [5], and [6] evaluated the ability of inertia emulation via power electronic devices. Adopting traditional energy storage systems (ESSs) for dampening the frequency oscillation tends to be the most widely used tactic for frequency regulation [7]. In our previous study [8], we proposed that instead of decommissioning the entire coal plant, the rotating mass of the decommissioned generator interfaced with the grid by means of a back-to-back converter, referred to as decoupled synchronous machine system (DSMS), can be employed as an energy storage unit to emulate the inertia with the help of an external frequency controller.

One of the major drawbacks in most of the current studies in this domain is that they largely depend on linearizing the system model in a tiny region surrounding a certain fixed operating point, followed by a linear control design. Unfortunately, such a structure does not ensure satisfactory performance when dealing with large frequency disturbances. Although there has been some research on the application of non-linear control design techniques to the stability control problem [1], [9], the availability of accurate non-linear models is highly challenging, thereby validating the need for data-driven non-linear control techniques [8], [10]. The Koopman operator-based control framework is purely data-driven and extremely simple to apply. It has shown incredible potential in the control of non-linear systems [11]–[15]. Koopman operator is an infinite-dimensional linear operator that can entirely unfold the dynamics of the underlying non-linear systems and take them forward in a linear manner [11]. The fundamental outline of Koopman operator theory is to effectively embed (or map) the original non-linear state space onto a higher dimensional space where its dynamics appear linear in the higher state space, followed by designing a linear control. Another major hurdle affecting traditional non-linear control design methods is the limits on input controls and states that the control design needs to consider. Typically, model predictive control (MPC) comes across as one of the few suitable methods in terms of constraints, since it avoids solving the

Manuscript received August 30, 2020; revised November 1, 2020; accepted December 17, 2020. Date of online publication September 10, 2021; date of current version October 14, 2021.

X. W. Li (corresponding author, email: xiawenli@vt.edu; ODCID: https://orcid.org/0000-0003-1627-8501), C. Mishra, and Y. J. Wang are with Dominion Energy, Richmond, VA, USA.

S. C. Chen is with Thorlabs Quantum Electronics., Jessup, MD, USA.

J. D. L. Ree is with Department of Electrical and Computer Engineering, Virginia Polytechnic Institute and State University, Blacksburg, VA, USA.

DOI: 10.17775/CSEEJPES.2021.02000

tricky Hamiltonian Jacobi-Bellman differential equation of the system with constraints, using the repeated solution of a finite-window optimization problem [16]–[18]. Facilitated by the Koopman operator, the original non-linear system embedded in the high-dimensional state space can be effectually controlled by a linear MPC.

An outline for the Koopman operator approximation and its application with MPC was proposed by Mezic *et al.* [11], which is applicable to a system where only input and output measurements are available. In such scenarios, internal states of the power system are mostly unobservable and immeasurable, which makes the forming of state space equations a hugely challenging task. Such a framework has been successfully applied to the DC motor speed control [11] as well as the complex non-linear flow control problems [12]. The applications of Koopman operator for the control of robotic systems under simulation and experimental environments were further analyzed in [13] and [14]. Hanke *et al*. applied the Koopman operator-based model predictive control (KMPC) in the field of power electronics, which is technically the first practical KMPC application of its kind [13]. The proposed method performed equivalent to the traditional model-based approaches. Furthermore, the application of KMPC was investigated for the transient stabilization problem for a non-linear power system model [10]. In [10], the average computational time for the control signal was approximately 10 ms, indicating the possibility of a real-time implementation in power system transient control. The concept of KMPC framework was also successfully applied to stabilize the power system frequency oscillation utilizing the proposed DSMS device in our previous study [8].

The prerequisite to constructing an approximation to Koopman operator tends to be the preference of embedding from the original non-linear state space to the new higher dimensional one, which simultaneously accomplishes linearization. From this perspective, Brunton illustrated time-delayed embedding to be a decent mapping option, which essentially is inspired by the classical Takens' theorem [19], [20]. Simply put, the inputs and outputs observed over a period of time can serve as the new coordinates. Noticeably, the two instrumental parameters that need to be tuned suitably in order to achieve fast and effective control are sampling time, denoted by τ, and embedding dimension D_{E}, representing the number of samples to be collected (going back in time).

This study primarily contributes to this domain by proposing a systematic method to optimize the instrumental time-delayed embedding parameters for the generation of Koopman operator and determining its success in making the KMPC framework more vigorously efficient in terms of frequency control against the various power system conditions, such as load and topology changes. This study illustrates how a KMPC-based frequency controller is capable of minimizing the frequency oscillation as well as amplify the critical clearing time by about 3 cycles in the IEEE 39-bus system. The proposed KMPC-based control follows a simple implementation process. It is model-free, completely data-driven, and can be trained offline. Once implemented, it can attain the same computational speed as the linear MPC methods. Yet, it upholds the possibility of integration with the traditional control strategies because it can convert a non-linear problem to a linear domain.

The rest of the paper is organized as follows: Section II provides the theoretical basis of the Koopman operator. Section III elucidates the algorithms for determining optimal embedding parameters of the input-output system. Section IV describes the mechanism of KMPC. Section V establishes the efficacy of the proposed framework with an application to the frequency control device DSMS in IEEE 39-bus system. Section VI presents the conclusions as well as the potential future work.

II. Koopman Operator Theory

A. Koopman Operator for Input-output System via Time-delayed Embedding

Consider the typical input-output system,

$$\begin{aligned} x_{k+1} &= f(x_k, u_k), \\ y_k &= h(x_k) \end{aligned} \tag{1}$$

where x_k is the system state, u_k is the control input, y_k is the measured output, and k is the timestamp. This discrete-time representation holds the advantage of being more realistic since the collected data from the real-world systems is usually derived in the form of discrete-time sampling.

In general, the states appear to be immeasurable while only certain functions of the states can be quantified. Furthermore, having a linear representation of the input-output dynamics simplifies the control design step to a great extent. Hence, in order to find the linear approximation of (1) with input-output data pairs, we firstly need to define the measurable states of the input-output system. This paper assumes the time-delayed coordinates as the states of (1), because the dynamics of x_k are unknown and the utilization of time-delayed measurements is classical in system identification theory [11]. The next section provides a comprehensive explanation for why the time-delayed coordinate is chosen. Let $\zeta_{D_{\mathrm{E}},\tau,k}$ denote the time-delayed coordinates, i.e., y and u measured over a time window as follows:

$$\begin{aligned} \zeta_{D_{\mathrm{E}},\tau,k} = \Big[&y_k^{\mathrm{T}}, y_{k-\tau}^{\mathrm{T}}, \ldots, y_{k-\tau n_{\mathrm{dy}}}^{\mathrm{T}}, u_{k-1}^{\mathrm{T}}, \\ &u_{k-\tau}^{\mathrm{T}}, \ldots, u_{k-\tau n_{\mathrm{du}}}^{\mathrm{T}}\Big]^{\mathrm{T}} \end{aligned} \tag{2}$$

where T represents the matrix transformation, n_{dy} and n_{du} represent the embedding dimensions of the output and input, respectively, $D_{\mathrm{E}} = [n_{\mathrm{du}}, n_{\mathrm{dy}}]$, and τ is the sampling time, i.e., the time gap between two successive measurements.

Next, in conformity with [20], the new states at time k denoted by z_k are a dictionary of functions g acting on to $\zeta_{D_{\mathrm{E}},\tau,k}$

$$z_k = g(\zeta_{D_{\mathrm{E}},\tau,k}) \tag{3}$$

where g is the user-defined observable (lifting) function, which forms the infinite-dimensional linear space. In this paper, g is chosen as:

$$g(\zeta_{D_{\mathrm{E}},\tau,k}) = \left[\zeta_{D_{\mathrm{E}},\tau,k},\, \zeta_{D_{\mathrm{E}},\tau,k}(1)_2,\ \text{constant}\right]^{\mathrm{T}} \tag{4}$$

where $\zeta_{D_{\mathrm{E}},\tau,k}(1)$ represents the embedded coordinate with the most recent input-output measurements, i.e., $\zeta_{D_{\mathrm{E}},\tau,k}(1) = [y_k^{\mathrm{T}}, u_{k-1}^{\mathrm{T}}]$. The constant is chosen to be 1 in this paper.

Koopman operator $\kappa = [\boldsymbol{A}, \boldsymbol{B}]^{\mathrm{T}}$ characterizes the trajectories linearly in the new state space z spanned by observable g, i.e.,

$$z_{k+1} = \boldsymbol{A} z_k + \boldsymbol{B} u_k \tag{5}$$

It is worth noting that u_k in the second term $\boldsymbol{B}u_k$ of (5) is not lifted by g in order to preserve invertibility between inputs of the transformed and the original system [11].

B. Solution of Koopman Operator

An approximation of the Koopman operator ($\boldsymbol{A}, \boldsymbol{B}$ matrix pair) for KMPC is acquired by solving the following linear regression problem:

$$\begin{aligned} \boldsymbol{X}_{\mathrm{lift}} &= [g(\zeta_{D_{\mathrm{E}},\tau,0}), \ldots, g(\zeta_{D_{\mathrm{E}},\tau,N-1})] \\ \boldsymbol{Y}_{\mathrm{lift}} &= [g(\zeta_{D_{\mathrm{E}},\tau,1}), \ldots, g(\zeta_{D_{\mathrm{E}},\tau,N})] \end{aligned} \tag{6}$$

where N is the total number of samples. By resolving the optimization problem as given in (7), the system in (5) is formed.

$$\min_{\boldsymbol{A}', \boldsymbol{B}'} \|\boldsymbol{Y}_{\mathrm{lift}} - \boldsymbol{A}\boldsymbol{X}_{\mathrm{lift}} - \boldsymbol{B}\boldsymbol{U}\|_F \tag{7}$$

where $||\cdot||_F$ denotes the Frobenius or the Euclidean norm. $\boldsymbol{U} = [u_1, \ldots, u_N]$ represents the matrix formed with the input signals. The numerical solution of (7) is given in [11].

III. Optimal Choice of Time-delayed Embedding Parameters

A. Takens' Theorem and Extension to Input-output Systems

Time-delayed embedding essentially aims to unfold the underlying unknown n-dimensional non-linear dynamics by undertaking sequential observation of measurements. Takens' theorem, the fundamental principle behind time-delayed embedding, ensures the authentic reconstruction of the dynamics of a system under certain conditions [19]. It was extended to the input-output system by reconstructing the time-delayed coordinates given in (2) using the time series data [21]. It was hypothesized by Casdagli [21] that the following relationship holds true:

$$\begin{gathered} y_{k+1} = F\left(\zeta_{D_{\mathrm{E}},\tau,k}\right) = \\ F\left(\left[y_k^{\mathrm{T}}, y_{k-\tau}^{\mathrm{T}}, \ldots, y_{k-\tau n_{\mathrm{dy}}}^{\mathrm{T}}, u_{k-1}^{\mathrm{T}}, u_{k-\tau}^{\mathrm{T}}, \ldots, u_{k-\tau n_{\mathrm{du}}}^{\mathrm{T}}\right]^{\mathrm{T}}\right) \end{gathered} \tag{8}$$

The results from [22], [23] essentially validate Casdagli's conjecture for embedding such systems. Nonetheless, constructing a time-delayed coordinate has two instrumental prerequisites: The delay time τ and the embedding dimension D_{E}. Section III. B introduces the algorithm adopted for determining τ, i.e., the time gap between two successive measurements. Section III. C presents the algorithm applied for calculating the optimal embedding dimension D_{E}, which is required to reconstruct the system. Figure 1 illustrates the procedure of constructing the time-delayed coordinate $\zeta_{D_{\mathrm{E}},\tau,k}$. This study aims at determining these parameters for designing a fast and effective KMPC method for the frequency control problem, using the previously proposed DSMS system [8].

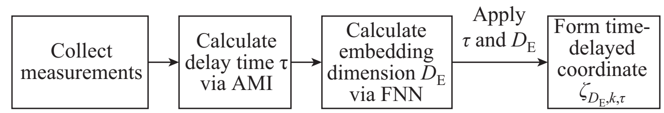

Fig. 1. Procedure of constructing $\zeta_{D_{\mathrm{E}},\tau,k}$.

B. Auto Mutual Information

To exemplify the importance of the delay time τ, a simple linear system $y = \sin(2\pi 60t)$ is selected in this section. According to the Nyquist theorem, a sampling rate of 2 × 60 Hz is sufficient to reconstruct the trajectory and thereby, a much higher sampling rate can be obtained. For a non-linear system, in order to obtain the accurate value of delay time, Fraser and Swinney proposed a method to compute the time gap between the points such that the delayed coordinates are as uncorrelated as possible [24]. In other words, they developed a way to quantify the dependence between the original time series data y_k and its time-shifted version $y_{k+\tau}$. This dependence is named as Auto Mutual Information [24] given by:

$$I(y_k, y_{k+\tau}) = \sum_{i,j} p_{ij}(\tau) \log\left(\frac{p_{ij}(\tau)}{p_i p_j}\right), k = 1, \ldots, N \tag{9}$$

where p_i is the probability that y_k is in bin i of the histogram drawn from the data points in y. $p_{ij}(\tau)$ is the probability that y_k is in bin i, while $y_{k+\tau}$ is in bin j. p_i and $p_{ij}(\tau)$ can be obtained by using histcounts function in Matlab. The optimal delay time τ is obtained at the first local minimum of Auto Mutual Information curve or when the curve reaches its threshold, defined as $1/e$ [25]. For the case of multidimensional time series, i.e., for more than one measurement, the simplest possible method referred to as uniform multivariate average mutual information method [26] can be employed. The idea is to present the mean of the delay time given by Auto Mutual Information curves of all the variables as the uniform delay. Vlachos and Kugiumtzis illustrated that by using this uniform method, the reconstructed state space exhibits a comparable quality to more complicated non-uniform multivariate methods [26]. In addition, depending upon the systems, several other methods could be used, such as the minimum time delay among all the variables, etc. [26].

C. Average False Nearest Neighbors

In the previous section, we obtained the sampling (delay) time between two given measurements via Auto Mutual Information algorithm. Now, this section presents the false nearest neighbors algorithm that is used to calculate the number of measurements needed to form the time-delayed coordinate, i.e., the minimum dimension D_{E} of the coordinate.

The principle behind the selection of these new state coordinates is that in order to preserve all the properties of the original dynamic system, the original states and the new states should possess a diffeomorphism [27] between them or simply put, differential invertible mapping. Since in the present study, we are mapping the original states onto a higher-dimensional linear space, the mapping from the original to the new space should serve as an embedding, i.e., there should be a continuous invertible mapping occurring between the original state space and its image in the new space. The false nearest neighbors (FNN) algorithm [28] is considered a standard method to determine the minimum time-delayed embedding dimension. The reason being that with an insufficient embedding dimension, the points that are not 'neighbors' in the original phase space become 'neighbors' in the new space as illustrated in a simple example in Fig. 2. The original state space is a three-dimensional cylinder containing points A, B, and C. In the insufficiently embedded two-dimensional space, where point A, B, and C are projected onto point A′, B′, and C′, respectively, point B′ will defectively be identified as the nearest neighbor of point A′.

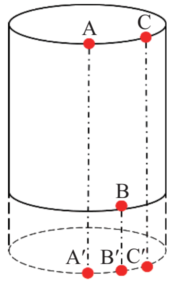

Fig. 2. Example of FNN with insufficient and sufficient embedding.

However, FNN depends on two user-defined thresholds for determining the true neighbors. The choice of the threshold is subjective, which can lead to different embedding dimensions [29]. A modified method referred to as average false nearest neighbors was introduced by Cao so as to avoid the above-mentioned subjective problem [29]. This algorithm was proposed for the autonomous system, which can easily be generalized to an input-output system [30]. Instead of using user-defined thresholds to determine if the nearest neighbor of each embedded point is true or false, Cao's algorithm evaluates $E_1(D_\mathrm{E})$ defined in (11), which is the average of change in distance between each point and its nearest neighbor after increasing the embedding dimension from D_E to $D_\mathrm{E}+1$. When D_E reaches its optimal value, $E_1(D_\mathrm{E})$ will cease further variations.

More accurately, we first define the change of distance between the embedded point $\zeta_{D_\mathrm{E},\tau,k}$ and its neighbor $\zeta^r_{D_\mathrm{E},\tau,k}$ going from dimension D_E to $D_\mathrm{E}+1$ as:

$$a_{D_\mathrm{E},k} = \frac{||\zeta_{D_\mathrm{E}+1,\tau,k} - \zeta^r_{D_\mathrm{E}+1,\tau,k}||}{||\zeta_{D_\mathrm{E},\tau,k} - \zeta^r_{D_\mathrm{E},\tau,k}||} \tag{10}$$

The average change of distances is defined as:

$$E_1(D_\mathrm{E}) = \frac{E(D_\mathrm{E}+1)}{E(D_\mathrm{E})} \tag{11}$$

where $E(D_\mathrm{E})$ is the mean of all $a_{D_\mathrm{E},k}$'s given by:

$$E(D_\mathrm{E}) = \frac{1}{N-\max(n_\mathrm{dy}, n_\mathrm{du})} \sum_{k=0}^{N-\max(n_\mathrm{dy},n_\mathrm{du})} a_{D_\mathrm{E},k} \tag{12}$$

IV. Koopman Model Predictive Control Using Optimal Time-delayed Embedding

In section II, the non-linear system is transformed into a linear system (5), which allows us to design the controller using classical linear control methodologies. In this study, MPC is adopted as the fundamental control algorithm. Yet, the power system control is non-linear in essence, which creates the non-convex problem, thereby posing challenges for its numerical solution. To formulate the optimization problem in a convex manner, [11] transforms the traditional non-linear MPC problem into Koopman MPC (13), which principally is a linear MPC without the loss of generality. In general, the model in (5) is used to predict the system evolution at each step k over the horizon with length N_p, and then applied to the optimization problem in (13) to resolve the optimal control u.

$$\begin{aligned}
\min_{u_k, z_k}\ & z_{N_\mathrm{p}}^\mathrm{T} \boldsymbol{Q}_{N_\mathrm{p}} z_{N_\mathrm{p}} + q_{N_\mathrm{p}}^\mathrm{T} z_{N_\mathrm{p}} + \sum_{k=0}^{N_\mathrm{p}-1} z_k^\mathrm{T} Q_i z_k + u_k^\mathrm{T} \boldsymbol{R}_i u_i + \\
& q_k^\mathrm{T} z_k + r_k^\mathrm{T} u_k \\
\text{s.t.}\quad & z_{k+1} = \boldsymbol{A} z_k + \boldsymbol{B} u_k, k = 0, \ldots, N_\mathrm{p}-1 \\
& y_k = \boldsymbol{C} z_k \\
& \boldsymbol{E}_k z_k + \boldsymbol{F}_k u_k \leqslant b_k, \\
& \boldsymbol{E}\boldsymbol{N}_\mathrm{p} z_{N_\mathrm{p}} \leqslant b_{N_\mathrm{p}}, \\
& z_0 = g\left(\zeta_{D_\mathrm{E},\tau,0}\right)
\end{aligned} \tag{13}$$

where $\boldsymbol{C}$ is a linear mapping from the new state space variable z_k to the original system output y_k. $\boldsymbol{C} = [\boldsymbol{I}, \boldsymbol{0}]$ after possible reordering of z_k. $\boldsymbol{Q}_k$ and $\boldsymbol{R}_k$ denote the positive semi-definite weighting matrices. $\boldsymbol{E}_k$, $\boldsymbol{F}_k$, and b_k are the state and input polyhedral constraints. (13) is transformed into a dense form (14), such that the rapid computation can be performed using quadratic programming (QP) solvers regardless of the size of the lifting.

$$\begin{aligned}
&\min_{\boldsymbol{U} \in \mathbb{R}^{mN_\mathrm{p}}} \boldsymbol{U}^\mathrm{T} \boldsymbol{H} \boldsymbol{U}^\mathrm{T} + z_0^\mathrm{T} \boldsymbol{G} \boldsymbol{U} \\
&\text{subject to } \boldsymbol{L}\boldsymbol{U} + \boldsymbol{M} z_0 \leqslant c \\
&\text{parameter } z_0 = g(x_k) \\
&\boldsymbol{U} = \left[u_0^\mathrm{T}, \ldots, u_{N_\mathrm{p}-1}^\mathrm{T}\right]^\mathrm{T}
\end{aligned} \tag{14}$$

where m is the dimension of input u. Refer [11] for the explicit transformation and definitions of $\boldsymbol{H}$, $\boldsymbol{G}$, $\boldsymbol{L}$, $\boldsymbol{M}$, and c. After it is transformed into (14), the formulation develops independent of the size of the lifting space [10]–[12]. As a result, within the same prediction window and with the identical inputs and states, the computational cost of solving (14) is comparable to that of solving a standard linear MPC. More importantly, the matrices utilized in (14) are derived from offline computation and hence, end up saving a lot of computation time. On the other hand, conventional ways of using MPC for non-linear systems requires the computation of matrices at each step [11] and thus the process of resolution tends to be substantially slower. These aforementioned details allow the utilization of the existing incredibly efficient QP solvers. In this study, structure-exploiting active-set QP solver 'qpOASES' [31] is utilized. Ferreau *et al.* demonstrates that the parametric active-set method is apt for applications that require a priori knowledge [31]. This method speeds up the QP solution and provides high accuracy as well. Ferreau *et al*. also showed that qpOASES outperform other popular academic and commercial QP solvers in small-to medium-scale convex studies [31].

The proposed framework is summarized in Algorithm 1. The construction of the KMPC framework is completed offline employing a large set of offline simulation data. Hence, the application of the KMPC method cannot be constrained by the linearization process.

Algorithm 1: Computation of time-delay embedding parameters for KMPC

1: Compute optimal τ^* for input and output using (9). Adopt the average τ for each variable.
2: **for** $k = 0, 2, \ldots, N$ **do**
3:    **for** $n_{\text{du}} = 1, \ldots, N_{\text{du}}$ and $n_{\text{dy}} = 1,\ \tau,\ N_{\text{dy}}$ **do**
4:       Construct delay embedding vector $\zeta_{D_{\text{E}},\tau,k}$ using (2)
5:       Compute $E_1(D_{\text{E}})$ using (10) to (12)
6:       Record $D_{\text{E}}^* = [n_{\text{du}}^*, n_{\text{dy}}^*]$ as minimum embedding dimension once $E_1(D_{\text{E}})$ stops change. Otherwise, go to 3.a.
7:    **end for**
8: **end for**
9: Adopt D_{E}^* and τ^* as the embedding parameters and solve (7) for $\boldsymbol{A}$, B
10: Substitute $\boldsymbol{A}$, B into KMPC (13). Solve (13) for u^* and apply $u^*(1)$ to the non-linear system at each step of control.

V. Case Study

A. DSMS Device

To test the efficiency of Algorithm I, the frequency regulation device DSMS proposed in [8] is utilized in this paper and the process is explained below.

The DSMS device is used to fully harness the advantage of the retired traditional unit for damping the frequency oscillation. Currently, an increasing number of traditional power plants have been replaced with renewable energy resources. Instead of dismantling the entire plant of the retired unit, the rotating mass of the generator can be converted into a flywheel to provide frequency support during disturbances, while the other parts, i.e., the governor and exciter can be eliminated.

DSMS consists of the rotating mass of the generator and an AC-DC-AC converter, as shown in Fig. 3. The working mechanism basically delivers active power to the grid when the frequency is low or absorbs active power from the grid when the frequency is high. Moreover, the DC-link voltage is utilized to assist in the frequency regulation, as shown in [32]. In other words, the DSMS device can curtail the magnitude of the frequency oscillation to stabilize the system.

KMPC controller is used to compute the amount of active power and DC-link voltage deviation needed to dampen the frequency oscillation. As shown in Fig. 3, the system enclosed inside the Blackbox is comprised of the DSMS device and the power grid. The commands of $P_{\text{e,ref}}$ and $dV_{\text{dc,ref}}$ of DSMS are the regulated inputs u for frequency control, while the output y is the grid side frequency. Despite the state equations of DSMS in (15), the mathematical equation of the entire Blackbox system tends to be tedious to derive, since there are numerous non-linear elements in the power grid, such as the battery energy system, transformers, etc.

$$
\begin{aligned}
L_{\text{r}}\frac{\mathrm{d}i_{\text{rd}}}{\mathrm{d}t} &= \omega_{\text{r}} L_{\text{r}} i_{\text{rq}} - R_{\text{r}} i_{\text{rd}} - v_{\text{rc}}^{\text{d}} \\
L_{\text{r}}\frac{\mathrm{d}i_{\text{rq}}}{\mathrm{d}t} &= -\omega_{\text{r}} L_{\text{r}} i_{\text{rd}} - R_{\text{r}} i_{\text{rq}} - v_{\text{rc}}^{\text{q}} + E_{\text{rq}} \\
\frac{\mathrm{d}\delta_{\text{r}}}{\mathrm{d}t} &= \omega_{\text{r}} \\
\frac{2H}{\omega_0}\frac{\mathrm{d}\omega_{\text{r}}}{\mathrm{d}t} &= -P_{\text{E}} \\
L_{\text{g}}\frac{\mathrm{d}i_{\text{gd}}}{\mathrm{d}t} &= \omega_{\text{g}} L_{\text{g}} i_{\text{gq}} - R_{\text{g}} i_{\text{gd}} - v_{\text{gc}}^{\text{d}} \\
L_{\text{g}}\frac{\mathrm{d}i_{\text{gq}}}{\mathrm{d}t} &= -\omega_{\text{r}} i_{\text{gd}} - R_{\text{g}} i_{\text{gq}} - v_{\text{gc}}^{\text{q}} + V_{\text{gq}} \\
\frac{\mathrm{d}v_{\text{dc}}}{\mathrm{d}t} &= \frac{1}{C_{\text{dc}}}\left(i_{\text{dc,r}} - i_{\text{dc,g}}\right)
\end{aligned} \tag{15}
$$

where E_{rq} is the generator constant voltage source behind the transient impedance $R_{\text{r}} + j\omega_{\text{r}} L_{\text{r}}$. i_{rdq} and $v_{\text{rc}}^{\text{dq}}$ represent the machine-side converter dq-axis currents and voltage, respectively. ω_{r} is the electrical rotor speed deviation relative to the nominal frequency ω_0 rad/s, δ_{r} is the rotor angle, and P_{E} is the active power output of the rotating mass. $R_{\text{g}} + j\omega_{\text{g}} L_{\text{g}}$ is

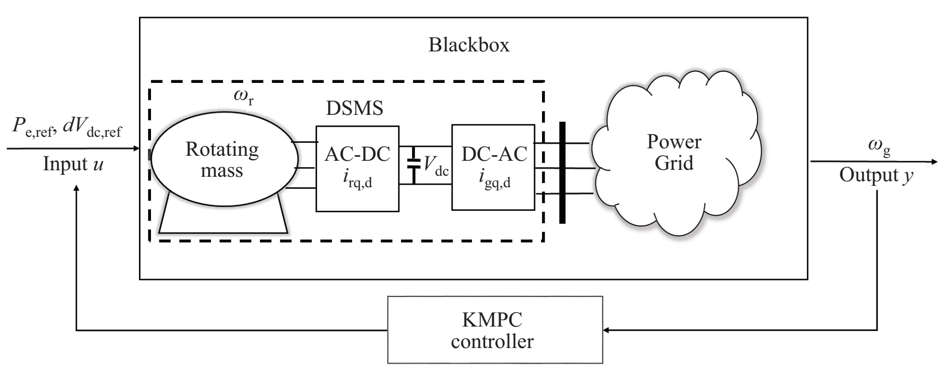

Fig. 3. Diagram of external KMPC controller of DSMS system.

the grid-side converter phase impedance. i_{gdq} and $v_{\mathrm{gc}}^{\mathrm{dq}}$ are the grid-side converter dq-axis currents and voltage, respectively. ω_{g} is the grid frequency. V_{gq} is the q-axis grid voltage, which is an external input to the system. The DC circuit is modeled by the equivalent DC capacitance C_{dc}, voltage v_{dc}, machine/grid-side DC currents $i_{\mathrm{dc,r}}$, and $i_{\mathrm{dc,g}}$. The power balance between AC and DC sides is as given in (16).

$$\begin{aligned} P_{\mathrm{E}} &= E_{\mathrm{rq}} i_{\mathrm{rq}} = v_{\mathrm{dc}} i_{\mathrm{dc}} \\ &= v_{\mathrm{rc}}^{\mathrm{q}} i_{\mathrm{rq}} + v_{\mathrm{rc}}^{\mathrm{d}} i_{\mathrm{rd}} = v_{\mathrm{gc}}^{\mathrm{q}} i_{\mathrm{gq}} + v_{\mathrm{gc}}^{\mathrm{d}} i_{\mathrm{gd}} = V_{\mathrm{gq}} i_{\mathrm{gq}} \end{aligned} \tag{16}$$

The internal control loops of the machine-side and the grid-side converters are given in Fig. 4 and Fig. 5, respectively. The derivations of converter state equations and the control loop, which can be found in [16], are not presented here since they do not represent the primary focus of this paper. By and large, the active power, reactive power, and the DC voltage references generate the references of the converter currents, which then provide the references of the converter voltages, namely duty cycles of the switching.

To test if the DSMS device can follow the commands precisely, a 0.6 p.u. step change of the active power command and a 0.2 p.u. step change of DC-link voltage command is applied, respectively. It can be seen from Fig. 6 and Fig. 7 that the DSMS device adheres to the commands quickly and accurately with reasonable overshoots [16].

B. KMPC Formulation of DSMS

In this section, the KMPC formulation of DSMS is presented. The KMPC controller issue is solved at each time step of the following optimization problem. The objective function is formulated to attain the optimal input $u = [P_{\mathrm{E}}, dV_{\mathrm{dc}}]$, to achieve the desired frequency z_k.

$$\begin{aligned} \min_{u_k} \sum_{k=0}^{N_{\mathrm{p}}-1} & \left(z_k^{ref} - z_k\right)^{\mathrm{T}} \boldsymbol{Q} \left(z_k^{ref} - z_k\right) + u_k^{\mathrm{T}} \boldsymbol{R} u_k \\ \text{s.t. } & z_{k+1} = \boldsymbol{A} z_k + \boldsymbol{B} u_k, k = 0, \ldots, N_{\mathrm{p}} - 1 \\ & y_k = \boldsymbol{C} z_k \\ & |P_{\mathrm{e}.k}| \leqslant b_k, \\ & |dV_{\mathrm{dc},k}| \leqslant a_k, \\ & z_0 = g\left(\zeta_{D_{\mathrm{E}},\tau,0}\right) \end{aligned} \tag{17}$$

where $\boldsymbol{Q}$ and $\boldsymbol{R}$ are the symmetric positive semi-definite weighting matrices. $\zeta_{D_{\mathrm{E}},\tau,0}$ denotes the time-delayed embedding coordinate at time step $k = 0$. b_k is the constraint for the control signals active power, while a_k is the constraint for

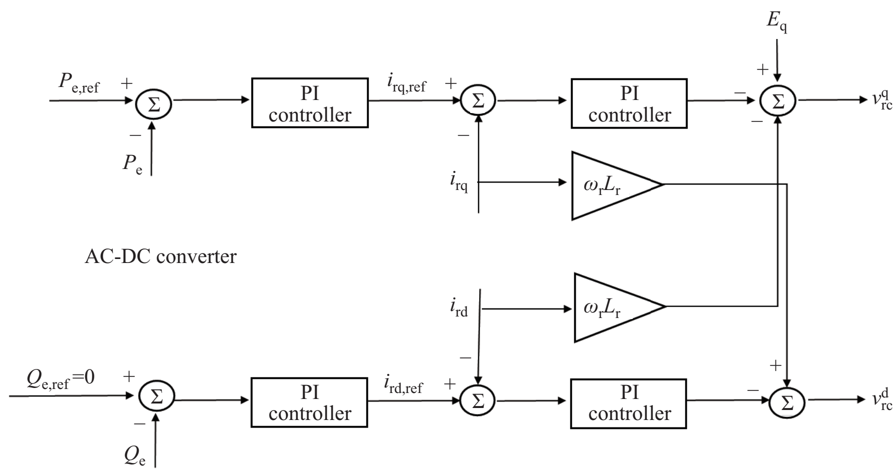

Fig. 4. Internal control loops of machine-side converter of DSMS.

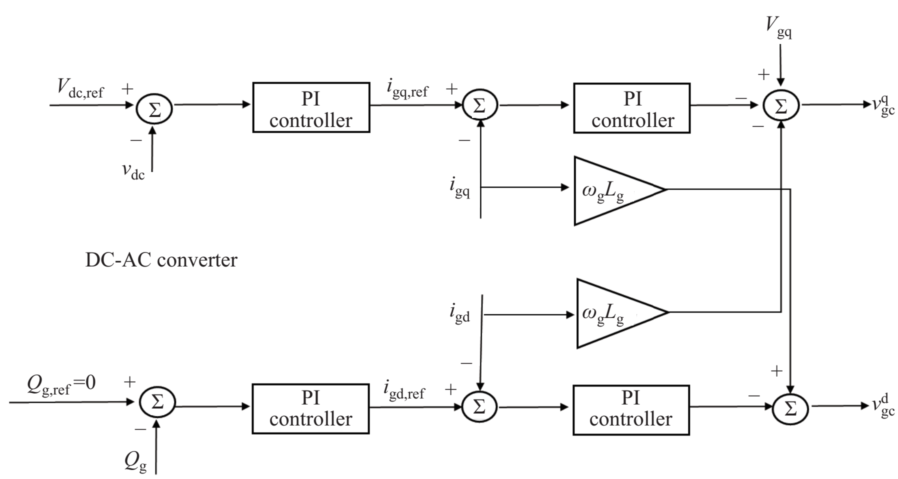

Fig. 5. Internal control loops of grid-side converter of DSMS.

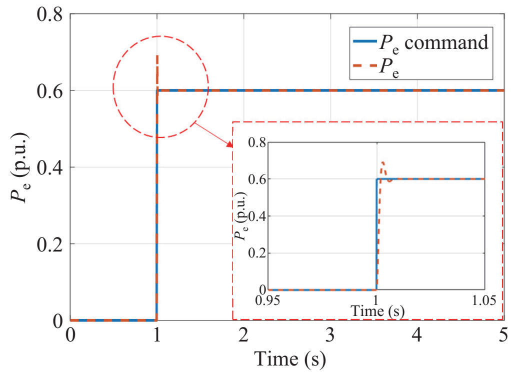

Fig. 6. DSMS response of active power command.

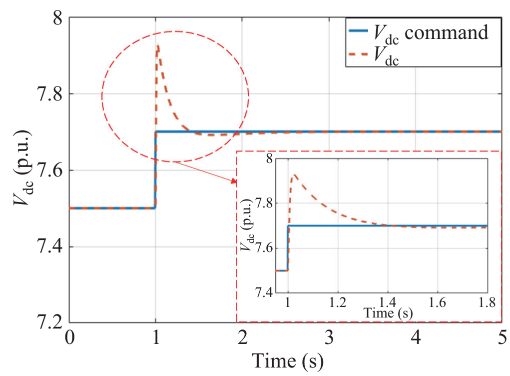

Fig. 7. SMS responses of DC-link voltage commands.

the control signal DC-link voltage variation. The entire optimization process is repeatedly solved in a 'receding horizon fashion', where only the first element of the input sequence u is applied at each instance.

C. Studied Systems

In this sub-section, the above-mentioned algorithm is discussed with respect to two power systems—the Kundur two-area system and the IEEE39-bus system. For each system, three different categories are analyzed, making a total of six cases. These three categories are:

- Original systems.
- Modified systems (without KMPC) – one conventional power plant replaced with the renewable generation resource modeled as the negative constant load (no frequency control capability).
- Modified systems (with KMPC) – adding the DSMS device with KMPC frequency controller to the second category.

1) Kundur Two-area System

The proposed algorithm is first tested in the Kundur two-area system, see Fig. 8. For the first case study, we replaced the generator at bus No. 3 by a negative constant load (passive IBR) and compared its performance with the scenario where that generator is converted into a DSMS device as proposed in [8].

a) Time-delayed Embedding Parameters

Data from 10^4 random eventualities with 0.01 s sampling time was collected using offline time-domain simulations in *Matlab/Simulink*. Note that $[P^*_{\mathrm{E}}, \Delta V^*_{\mathrm{dc}}]$ is constrained within [$\pm$ 0.1 p.u., $\pm$ 0.1 p.u.]. Following the algorithm given in Algorithm 1, we first drew the Auto Mutual Information curve for the output local frequency and the inputs P^*_{E} and ΔV^*_{dc}. The optimal time lag for frequency, P^*_{E} and ΔV^*_{dc} is determined through the elbow of the Auto Mutual Information curve, i.e., 9, 5, and 5 respectively. The average time lag for the three numbers is 6, which leads to the final τ, i.e., 0.06 s, see Fig. 9.

Applying τ^* to the extended Cao's algorithm yields Fig. 10. The white dotted line signifies the candidates of the minimum $[n_{\mathrm{dy}}, n_{\mathrm{du}}]$ combinations. $[n_{\mathrm{dy}}, n_{\mathrm{du}}] = [8, 8]$ is chosen due to the corresponding low root mean square error method (RMSE). In general, the state space of a practical power system is massive. However, the embedding dimension chosen is based on the dimensionality of the region in state space to which the system dynamics are constrained for the given set of events being analyzed (local), which tends to be much lower. In other words, for a local disturbance even in a large-scale system, the measurement data is ranked low, which restricts the optimal embedding dimension obtained to a great extent, thus making our approach even more practical.

b) Frequency Prediction

Now, based on Algorithm 1, the Koopman operator-based linear system (3) can be constructed by resolving (9) using the embedding parameters derived from the previous sub-section. To validate the accuracy of the linear system, 200 random frequency trajectories were investigated. The average RMSE with 4.2 s prediction window over those trajectories was calculated. To justify the optimal embedding dimension, the

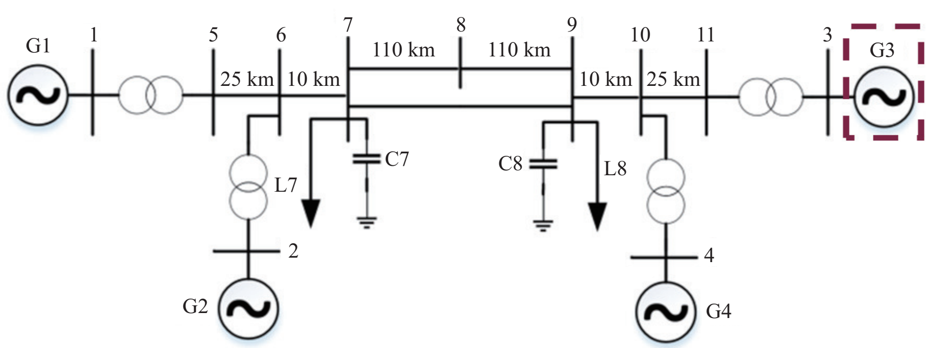

Fig. 8. Kundur two-area system diagram.

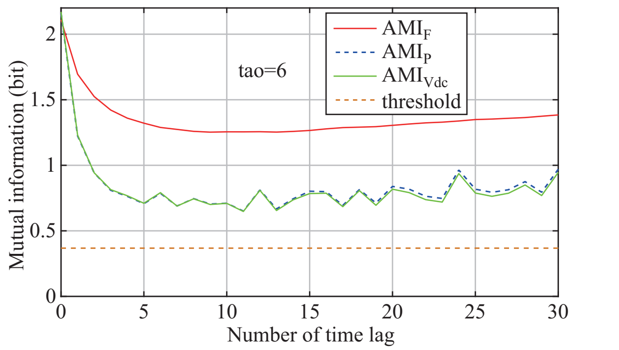

Fig. 9. Auto mutual information curve for delay time of Kundur two-area system.

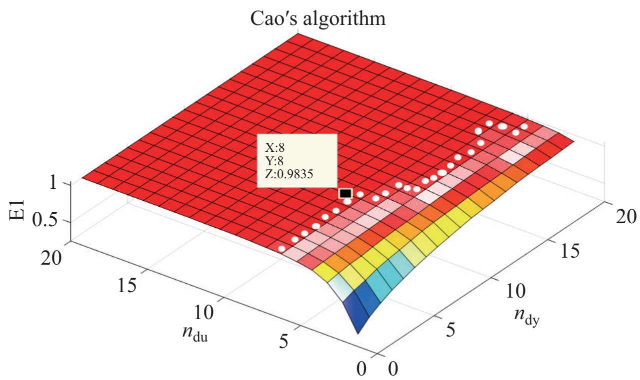

Fig. 10. FNN for embedding dimension of Kundur two-area system.

frequency predictions were also performed with another two sets of embedding dimensions; one set consisted of insufficient embedding dimension, namely non-optimal, whilst the other set possessed more than sufficient, namely sub-optimal. The comparison between the various embedding dimensions is given in Table I. As indicated by the RMSE in Table I, $[n_{dy}, n_{du}] = [4, 4]$ is incapable of providing a sufficient space to unfold the dynamics of the system. Even though $[n_{dy}, n_{du}] = [8, 8]$ and $[n_{dy}, n_{du}] = [20, 20]$ both possess similar low RMSE, the set with lesser embedding is preferred due to faster control and lesser computational complicacy.

TABLE I
RMSE OF DIFFERENT EMBEDDING DIMENSION, KUNDUR TWO-AREA SYSTEM

$[n_{dy}, n_{du}]$	RMSE
Optimal [8, 8]	1.54%
Sub-optimal [20, 20]	1.37%
Non-optimal [4, 4]	20.3%

It is hypothesized that in the lifting functions g in (4), the inclusion of higher degree polynomials of the embedded coordinate $\zeta_{D_E,\tau,k}$, which comprises of the most recent input and output measurements, can better portray the underlying non-linear dynamics of the original system. To study its effects, we compared the frequency prediction accuracy (RMSE) for different higher degree orders included in the lifting function. As shown in Table II, after the optimal embedding dimension is accomplished, the prediction in the non-linear term in this study remains more or less the same.

TABLE II
RMSE OF FREQUENCY PREDICTION WITH OR WITHOUT NON-LINEAR TERM IN LIFTING FUNCTION, KUNDUR TWO-AREA SYSTEM

RMSE Without $\|\zeta_{D_E,\tau,k}\|_2$	RMSE With $\|\zeta_{D_E,\tau,k}\|_2$	RMSE With $\|\zeta_{D_E,\tau,k}\|_{[2,3,4]}$
1.60%	1.54%	1.26%

c) Frequency Controller

To test the performance of the proposed Koopman operator-based MPC framework against large frequency disturbances, a three-phase-to-ground fault at bus No. 8 is applied at 1 s. The fault results in tripping one of the double line connecting area 1 and 2, which was then reclosed at 6 s. Figure 11 demonstrates that with the control signals in Fig. 12, the system with KMPC efficiently enhances the frequency stability by damping more oscillation. The average computational time of the KMPC of this frequency control is 1.2 ms running on an Intel Core i7-8750 CPU @ 2.20 GHz, RAM 16 GB processor and the Accelerator mode in Simulink.

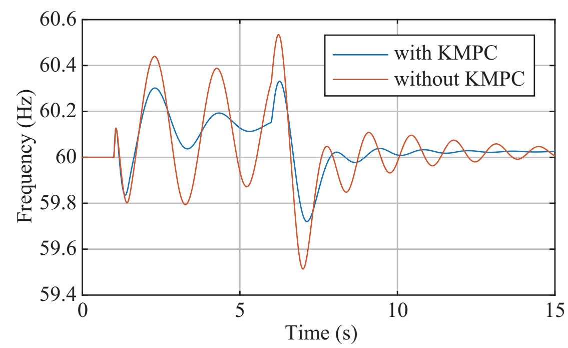

Fig. 11. Frequency responses with/without KMPC, Kundur two-area system.

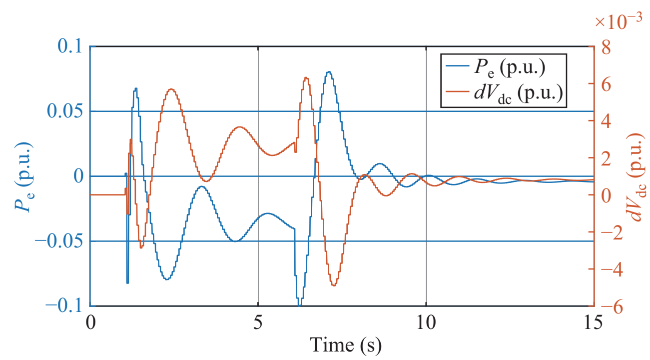

Fig. 12. KMPC control signals, Kundur-two area system.

d) Robustness Test

To test the robustness of the controller, we applied various system topologies. The transmission lines connecting area 1 and 2 are chosen as the analyses areas, because this region forms the most critical line in this system. We applied different line impedances of the double lines. As indicated from Fig. 13, KMPC can dampen the oscillation with critical changes in the system.

e) Critical Clearing Time

To further evaluate the KMPC performance, this section demonstrates the efficacy of the proposed controller for enhancing the transient stability of the system by comparing critical clearing time (CCT) values for the same fault. A three-phase fault is applied at bus 9 in the system before and after implementing KMPC, respectively. The results listed in Table III illustrate that CCT is increased by 0.05 s.

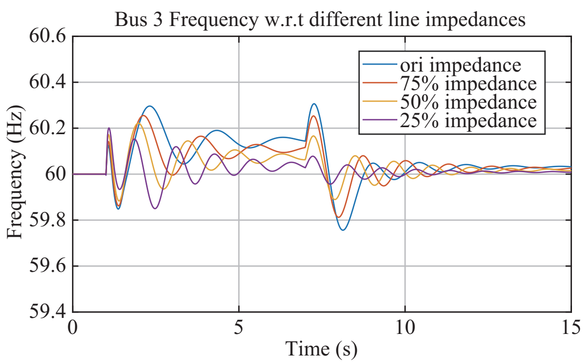

Fig. 13. Frequency and voltage responses of generator 3 with different double-line impedances; Kundur two-area system.

TABLE III
CCT COMPARISONS, KUNDUR TWO-AREA SYSTEM

System	CCT (s)
Original Kundur two-area systems	0.31 s
KMPC system	0.36 s

2) IEEE 39-Bus System

The proposed algorithm is evaluated through a larger system, i.e., the IEEE39-bus system given in Fig. 14. Similarly, generator at bus No. 30 is replaced by the negative constant load along with the DSMS device.

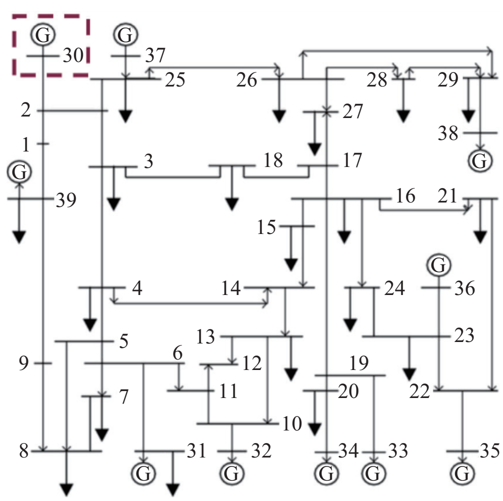

Fig. 14. IEEE39-bus system diagram.

a) Time-delayed Embedding Parameters

In this case, data from 10^4 random eventualities was again collected offline. $[P_{\mathrm{E}}^*, \Delta V_{\mathrm{dc}}^*]$ is constrained within [$\pm$ 0.5 p.u., $\pm$ 0.2 p.u.]. The Auto Mutual Information curves for the output local frequency and the inputs, P_{E}^*, and ΔV_{dc}^* are given in Fig. 15. The average time lag for the three numbers is 7, resulting in the final τ, i.e., 0.07 s. Following the same steps and mechanism as for the Kundur two-area case study, $[n_{\mathrm{dy}}, n_{\mathrm{du}}] = [18, 18]$ is chosen, see Fig. 16.

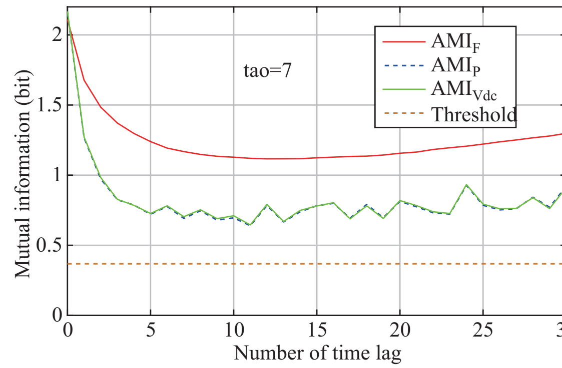

Fig. 15. Auto Mutual Information curve for delay time of IEEE39-bus system.

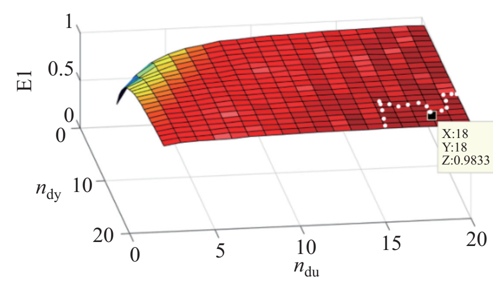

Fig. 16. FNN for embedding dimension of IEEE39-bus system.

b) Frequency Prediction

Following Algorithm 1, the Koopman operator-based linear system can be reconstructed with the embedding parameters obtained from the previous sub-section. Analogous to the Kundur two-area case study, the comparison between different embedding dimensions is performed, see Table IV. As indicated by this Table, $[n_{\mathrm{dy}},\ n_{\mathrm{du}}] = [3,\ 3]$ is incapable of providing a sufficient space to unfold the dynamics of the system. Even though $[n_{\mathrm{dy}},\ n_{\mathrm{du}}] = [18,\ 18]$ and $[n_{\mathrm{dy}},\ n_{\mathrm{du}}] = [30,\ 30]$ both have similar low RMSE value, the set with lesser embedding is preferred due to faster control algorithm.

TABLE IV
RMSE OF DIFFERENT EMBEDDING DIMENSION, IEEE39-BUS SYSTEM

$[\boldsymbol{n}_{\mathrm{dy}}, \boldsymbol{n}_{\mathrm{du}}]$	RMSE
Optimal [18, 18]	1.86%
Sub-optimal [30, 30]	1.51%
Non-optimal [3, 3]	99.45%

As shown in Table V, when the optimal embedding dimension value is reached, the non-linear term ceases to change the prediction largely, in this study.

c) Frequency Controller

A three-phase-to-ground fault at bus No. 25 is applied at 1 s, which trips the line connecting buses 25 and 26. Figure 17 illustrates that the system with KMPC efficiently enhances the frequency stability with the control signals in Fig. 18. The average computational time of the KMPC in this case is 3 ms under the same simulation environment as the Kundur two-area case study.

TABLE V
RMSE OF FREQUENCY PREDICTION WITH OR WITHOUT NONLINEAR TERM IN LIFTING FUNCTION, IEEE39-BUS SYSTEM

RMSE without $\|\zeta_{D_E,\tau,k}\|_2$	RMSE with $\|\zeta_{D_E,\tau,k}\|_2$	RMSE with $\|\zeta_{D_E,\tau,k}\|_{[2,3,4]}$
1.93%	1.86%	1.53%

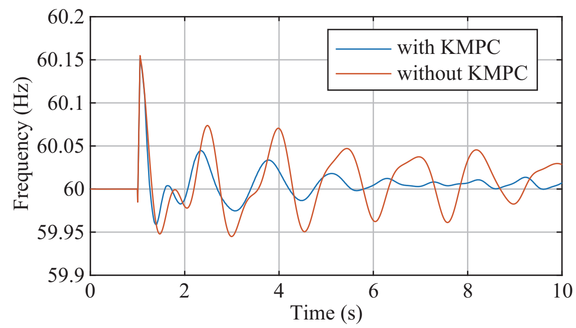

Fig. 17. Frequency responses with/without KMPC, IEEE39-bus system.

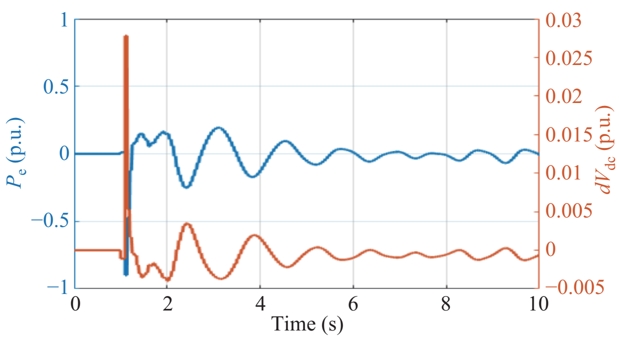

Fig. 18. KMPC Control signals, IEEE39-bus system.

d) Robustness Tests

In this section, we analyze the robustness of the controllers when operating condition changes. The first scenario is of the robustness against load changes. The largest load at bus 39 (over 1000 MW) is reduced by half, while the second largest load at bus 20 (over 600 MW) is doubled. The second scenario is of the robustness against the change of transmission line impedance/network topology. We picked the line connecting 21 to 22, which happens to be a major transmission corridor for this system. On top of the previously defined load changes, the impedance of the selected line increases to 500%. According to the frequency responses of the above scenarios given in Fig. 19 and Fig. 20, the controller is still capable of handling large frequency oscillation under different operating conditions.

D. Critical Clearing Time

A three-phase fault is applied at bus 3 in the original nonlinear system and the system with KMPC, respectively, so as to evaluate the CCT of both the systems. The CCT is witnessed to increase by approximately 2 cycles, see Table VI.

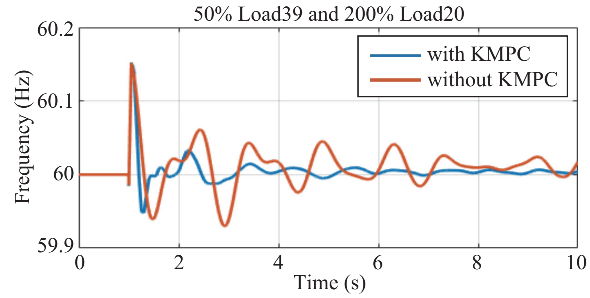

Fig. 19. Frequency responses with/without KMPC for the first scenario.

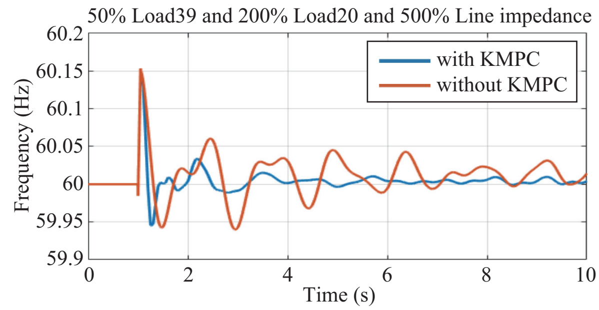

Fig. 20. Frequency responses with/without KMPC for the second scenario.

TABLE VI
CCT COMPARISON, IEEE39-BUS SYSTEM

System	CCT (s)
Original IEEE39-bus system	0.20 s
KMPC system	0.24 s

VI. CONCLUSION

A model-free methodology is proposed for determining the optimal measurements of the parameters of time-delayed embedding coordinate used for Koopman operator approximation. The methodology is utilized to obtain the linear approximation of a non-linear system with only input-output measurements, while none of the state measurements are given. To test the efficacy of the proposed method, we employed the Kundur two-area and the IEEE 39-bus system cases, wherein the energy storage device DSMS serves as the frequency control device, whose inputs are the active power and DC-link voltage command, whilst output is the terminal frequency. The proposed Koopman-operator based framework exhibits promising performance in predicting the frequency trajectories. Furthermore, KMPC is capable of dampening the frequency oscillation under different system operating conditions.

The proposed framework delivers satisfactory performance in the above-mentioned cases. However, the data driven nature also makes it prone to noise and corrupted data in real-field measurements, and hence, it requires better data preprocessing and screening for real-world deployment. Besides, the operating conditions of the power system may vary dramatically in case of occurrence of large disturbances. If these conditions are not included in the offline studied cases, the offline trained KMPC may not act fast enough to adapt to the new online cases. Furthermore, this framework can be applied to the system with real-time data. In addition to the well-established performance for transient frequency control, KMPC also tends to be potentially useful for other large time-scale applications, such as economic dispatch, active power regulation, etc., which could be a prospective research subject.

REFERENCES

[1] Y. Z. Sun, Z. S. Zhang, G. J. Li, and J. Lin, "Review on frequency control of power systems with wind power penetration," in *2010 International Conference on Power System Technology*, 2010, pp. 1–8, doi: 10.1109/POWERCON.2010.5666151.

[2] M. Dreidy, H. Mokhlis, and S. Mekhilef, "Inertia response and frequency control techniques for renewable energy sources: a review," *Renewable and Sustainable Energy Reviews*, vol. 69, pp. 144–155, Mar. 2017, doi: 10.1016/j. rser.2016.11.170.

[3] M. H. Variani and K. Tomsovic, "Distributed automatic generation control using flatness-based approach for high penetration of wind generation," *IEEE Transactions on Power Systems*, vol. 28, no. 3, pp. 3002–3009, Aug. 2013, doi: 10.1109/TPWRS.2013.2257882.

[4] P. P. Zarina, S. Mishra, and P. C. Sekhar, "Deriving inertial response from a non-inertial PV system for frequency regulation," in *2012 IEEE International Conference on Power Electronics*, *Drives and Energy Systems* (*PEDES*), Bengaluru, 2012, pp. 1–5, doi: 10.1109/PEDES.2012.6484409.

[5] H. Liu, D. Sun, F. Zhao, Y. Tian, P. Song and X. Cheng, "The influence of virtual synchronous generators on low frequency oscillations," in *CSEE Journal of Power and Energy Systems*, doi: 10.17775/CSEE-JPES.2020.01700.

[6] H. Fang and Z. Yu, "Improved virtual synchronous generator control for frequency regulation with a coordinated self-adaptive method," in *CSEE Journal of Power and Energy Systems*, doi: 10.17775/CSEE-JPES.2020.01950.

[7] L. Miao, J. Y. Wen, H. L. Xie, C. Y. Yue, and W. J. Lee, "Coordinated control strategy of wind turbine generator and energy storage equipment for frequency support," *IEEE Transactions on Industry Applications*, vol. 51, no. 4, pp. 2732–2742, Jul. /Aug. 2015, doi: 10.1109/TIA.2015.2394435.

[8] X. W. Li, J. De La Ree, and C. Mishra. "Frequency control of decoupled synchronous machine using Koopman operator based model predictive," in *2019 IEEE Power* & *Energy Society General Meeting* (*PESGM*), 2019, pp. 1–5.

[9] Q. Lu, S. W. Mei, W. Hu, F. F. Wu, Y. X. Ni, and T. L. Shen, "Nonlinear decentralized disturbance attenuation excitation control via new recursive design for multi-machine power systems," *IEEE Transactions on Power Systems*, vol. 16, no. 4, pp. 729–736, Nov. 2001, doi: 10.1109/59.962419.

[10] M. Korda, Y. Susuki, and I. Mezić, "Power grid transient stabilization using Koopman model predictive control," *IFAC-PapersOnLine*, vol. 51, no. 28, pp. 297–302, Mar. 2018.

[11] M. Korda and I. Mezić, "Linear predictors for nonlinear dynamical systems: Koopman operator meets model predictive control," *Automatica*, vol. 93, pp. 149–160, Jul. 2018, doi: 10.1016/j.automatica.2018.03.046.

[12] H. Arbabi, M. Korda and I. Mezić, "A Data-Driven Koopman Model Predictive Control Framework for Nonlinear Partial Differential Equations," *2018 IEEE Conference on Decision and Control (CDC)*, 2018, pp. 6409-6414, doi: 10.1109/CDC.2018.8619720.

[13] S. Hanke, S. Peitz, O. Wallscheid, S. Klus, J. Böcker, and M. Dellnitz, "Koopman operator-based finite-control-set model predictive control for electrical drives," arXiv preprint, arXiv:1804.00854 [math. OC], 2018.

[14] I. Abraham, G. De La Torre, and T. D. Murphey, "Model-based control using koopman operators," arXiv preprint, arXiv: 1709.01568, 2017 [cs. RO].

[15] D. Bruder, X. Fu, R. B. Gillespie, C. D. Remy and R. Vasudevan, "Data-Driven Control of Soft Robots Using Koopman Operator Theory," in *IEEE Transactions on Robotics*, vol. 37, no. 3, pp. 948-961, June 2021, doi: 10.1109/TRO.2020.3038693.

[16] I. Markus, "Voltage source converter based HVDC-modelling and coordinated control to enhance power system stability," Doctoral dissertation, Dep. of Inform. Technol. Electrical Eng., ETH Zurich, Zurich, 2015.

[17] A. Fuchs, S. Mariéthoz, M. Larsson, and M. Morari, "Grid stabilization through VSC-HVDC using wide area measurements," in *2011 IEEE Trondheim PowerTech*, 2011, pp. 1–6.

[18] P. M. Namara, R. R. Negenborn, B. De Schutter, and G. Lightbody, "Optimal coordination of a multiple HVDC link system using centralized and distributed control," *IEEE Transactions on Control Systems Technology*, vol. 21, no. 2, pp. 302–314, Mar. 2013.

[19] F. Takens, "Detecting strange attractors in turbulence," in *Dynamical Systems and Turbulence, Warwick 1980*, vol. 898, D. Rand and L. S. Young, Eds. Berlin, Heidelberg: Springer, 1981, pp. 366–381.

[20] S. L. Brunton, B. W. Brunton, J. L. Proctor, E. Kaiser, and J. N. Kutz, "Chaos as an intermittently forced linear system," *Nature Communications*, vol. 8, no. 1, pp. 19, May 2017.

[21] M. Casdagli, "A dynamical systems approach to modeling input-output systems," in *Nonlinear Modeling and Forecasting, Santa Fe Institute Studies in the Sciences of Complexity*, M. Casdagli and S. Eubank, Eds. Redwood City: Addison-Wesley Publishing Co, 1992, pp. 265–265.

[22] J. Stark, "Delay embeddings for forced systems. I. deterministic forcing," *Journal of Nonlinear Science*, vol. 9, no. 3, pp. 255–332, Jun. 1999, doi: 10.1007/s003329900072.

[23] J. Stark, D. S. Broomhead, M. E. Davies, and J. Huke, "Delay embeddings for forced systems. II. stochastic forcing," *Journal of Nonlinear Science*, vol. 13, no. 6, pp. 519–577, Dec. 2003, doi: 10.1007/s00332-003-0534-4.

[24] A. M. Fraser and H. L. Swinney, "Independent coordinates for strange attractors from mutual information," *Physical Review A*, vol. 33, no. 2, pp. 1134–1140, Feb. 1986.

[25] S. Wallot and D. M?nster, "Calculation of average mutual information (AMI) and false-nearest neighbors (FNN) for the estimation of embedding parameters of multidimensional time series in Matlab," *Frontiers in Psychology*, vol. 9, pp. 1679, Sept. 2018, doi: 10.3389/fpsyg.2018.01679.

[26] I. Vlachos and D. Kugiumtzis, "State space reconstruction from multiple time series," in *Topics on Chaotic Systems-Selected Papers from CHAOS 2008 International Conference*, Chania, Crete, Greece, 2009, pp. 378–387, doi: 10.1142/9789814271349_0043.

[27] J. M. Lee, "Smooth manifolds," in *Introduction to Smooth Manifolds*, vol. 218, J. M. Lee, Ed. New York: Springer, 2003, pp. 1–29.

[28] M. B. Kennel, R. Brown, and H. D. I. Abarbanel, "Determining embedding dimension for phase-space reconstruction using a geometrical construction," *Physical Review A*, vol. 45, no. 6, pp. 3403–3411, Mar. 1992, doi: 10.1103/PhysRevA.45.3403.

[29] L. Y. Cao, "Practical method for determining the minimum embedding dimension of a scalar time series," *Physica D*: *Nonlinear Phenomena*, vol. 110, no. 1–2, pp. 43–50, Dec. 1997, doi: 10.1016/S0167-2789(97)00118-8.

[30] D. M. Walker and N. B. Tufillaro, "Phase space reconstruction using input-output time series data," *Physical Review E*, vol. 60, no. 4, pp. 4008–4013, Oct. 1999, doi: 10.1103/PhysRevE.60.4008.

[31] H. J. Ferreau, C. Kirches, A. Potschka, H. G. Bock, and M. Diehl, "qpOASES: a parametric active-set algorithm for quadratic programming," *Mathematical Programming Computation*, vol. 6, no. 4, pp. 327–363, Dec. 2014, doi: 10.1007/s12532-014-0071-1.

[32] A. Junyent-Ferr, Y. Pipelzadeh, and T. C. Green, "Blending HVDC-link energy storage and offshore wind turbine inertia for fast frequency response," *IEEE Transactions on Sustainable Energy*, vol. 6, no. 3, pp. 1059–1066, Jul. 2015, doi: 10.1109/TSTE.2014.2360147.

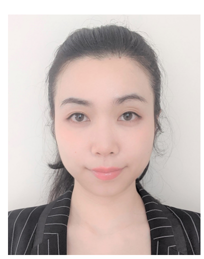

Xiawen Li received the Bachelor degree at Huazhong University of Science and Technology, China in 2013. She received the master degree from Newcastle University, UK in 2014. She received the Ph.D. degree from Virginia Polytechnic Institute and State University in 2019. Her employment experience included PJM Interconnection LLC and are currently an Engineer III in Dominion Energy. Her research focus includes power quality analysis, renewable integration, reactive power planning, electromagnetic analysis and blackstart.

Chetan Mishra (S'14–M'18) received the Bachelor of Technology (B-Tech) degree in Electrical Engineering from Indian Institute of Technology (BHU), Varanasi (India) in 2012 and the M.S. and Ph.D. degrees in Electrical Engineering from Virginia Tech, Blacksburg in 2014 and 2017. He is an Engineer in the Engineering Analytics and Modeling Group at Dominion Energy. His research interests include direct methods for transient stability assessment, renewables, nonlinear control and synchrophasor analytics.

Shichao Chen received the B.S. degree in Electronic Engineering from Tsinghua University, Beijing, China, in 2013, and the Ph.D. degree in Electrical Engineering from the Bradley Department of Electrical and Computer Engineering, Virginia Tech, Blacksburg, VA, USA, in 2019. His research focus is in developing highly sensitive imaging systems and associated signal processing algorithms. He is currently a Research Scientist in Thorlabs Quantum Electronics.

Yajun Wang received the B.Sc. and M.Sc. degrees from the School of Electrical Engineering, Wuhan University, Wuhan, China, in 2012 and 2014, respectively, and the Ph.D. degree in Electrical Engineering from the University of Tennessee, Knoxville, TN, USA, in 2019. She is currently working with Dominion Energy Virginia, Richmond, VA, USA, as a Senior Power System Engineer. Her research interests are big data analytics, power system stability and control, system restoration, energy storage systems, electric vehicles, and DER integration.

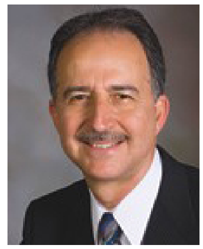

Jaime De La Ree received the B.S. degree from University of Monterrey, Mexico in 1980. He received master degree from University of Pittsburgh, USA in 1981. He received the Ph.D. degree from Virginia Tech, USA, in 1984. His research interest is Power engineering. He is currently the Associate Professor and Assistant Department Head of Department of Electrical and Computer Engineering, Virginia Tech.